Geomorphology 488 (2025) 109977

Contents lists available at ScienceDirect

Geomorphology

journal homepage: www.journals.elsevier.com/geomorphology

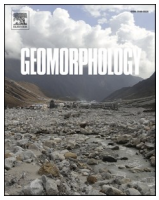

Rainfall overpowers tidal forcing in driving upper tidal flat erosion and channel evolution

Shang Yu [a], Fan Xu [a,*], Weiming Xie [a], Xianye Wang [a], Chunyan Zhu [a], Qing Yuan [a], Haisheng Yu [a], Zhonghao Zhao [a], Yijie Zhang [a], Zhengbing Wang [b,c], Giovanni Coco [d], Qing He [a]

[a] State Key Laboratory of Estuarine and Coastal Research, East China Normal University, Shanghai 200241, China
[b] Faculty of Civil Engineering and Geosciences, Section of Hydraulic Engineering, Delft University of Technology, Stevinweg 1, 2628 CN, P.O. Box 5048, 2600, GA, Delft, the Netherlands
[c] Deltares, Rotterdamseweg 185, P.O. Box 177, 2600 MH Delft, the Netherlands
[d] Faculty of Science, University of Auckland, 23 Symonds Street, Auckland 1010, New Zealand

A B S T R A C T

Tidal flats are critical coastal ecosystems, with their geomorphic characteristics traditionally understood to be primarily influenced by tidal, wave, and storm forces. This study investigates the impact of rainfall on the morphodynamics of upper tidal flats by combining hydrodynamic-sediment data, meteorological rainfall records, and video monitoring at the Chongming Dongtan tidal flat in the Yangtze River Estuary, China. We show that rainfall significantly increases suspended sediment transport and accelerates tidal channel elongation. Notably, rainfall events—though occurring during only 25 % of observed tidal inundation periods—accounted for 62 % of cumulative net sediment transport. This disproportionate efficiency compared to tidal forcing stems from the rainfall-induced hydraulic connectivity between expansive supratidal areas and tidal channels, where concentrated runoff convergence intensifies scour dynamics. These findings challenge the traditional view of tidal flat dynamics, suggesting that rainfall is a more influential driver of morphodynamic change than previously recognized.

1. Introduction

Tidal flat landscapes are crucial to coastal ecosystems and human communities, serving as natural barriers against storm surges and erosion, providing habitats for diverse species, and supporting essential ecological processes like nutrient cycling and carbon storage (Allen, 2000; Murray et al., 2019; Temmerman et al., 2013). As dynamic landscapes shaped by the interactions between hydrodynamic, sedimentary, and atmospheric forces (Fagherazzi et al., 2006; Friedrichs, 2012; Mariotti and Fagherazzi, 2010), tidal flats also act as sensitive indicators of environmental shifts, such as rising sea levels and declining sediment supply (Fivash et al., 2023; Mariotti and Fagherazzi, 2013). Therefore, studying the morphological evolution of tidal flats is vital for understanding these ongoing changes, their potential impacts, and how these landscapes may respond to natural forces and human activities.

The morphological evolution of tidal flats has been typically studied through the monitoring of hydrodynamic and sediment transport processes, supplemented by periodic topographic surveys (Fagherazzi and Priestas, 2010; Gong et al., 2017; Pieterse et al., 2016; Sun et al., 2024a; Talke and Stacey, 2008). However, direct observation of continuous morphological changes is often impractical under standard monitoring conditions (Tseng et al., 2017). Field studies usually rely on deploying instrumented frames on tidal flats and retrieving data after a set observation period (Andersen et al., 2006; Belliard et al., 2019; Gong et al., 2017; Hu et al., 2015; Ly and Huang, 2022; Pethick, 1981). This approach leaves gap in capturing the dynamic, real-time morphological response of tidal flats, as it lacks a “fixed eye” to continuously record morphological changes alongside the instrumentation. As a result, establishing process-response relationships between hydrodynamic forcing, sediment transport patterns, and resultant morphological changes remains challenging, particularly at the event scale where rapid geomorphic adjustments may occur.

This observational limitation may have biased research focus toward prototypical coastal forces shaping tidal flats. For example, wave action is typically considered to be a significant erosive force (Fagherazzi and Wiberg, 2009; Friedrichs and Perry, 2001; Green and Coco, 2014), while tidal currents are essential to the long-term stability of the flat (Friedrichs and Aubrey, 2011; Rinaldo et al., 1999; Seminara et al., 2004) and the development of drainage systems, i.e., tidal networks (Coco et al., 2013; Rinaldo et al., 1999; Seminara et al., 2004). Meanwhile, episodic events like storms are increasingly acknowledged for their dramatic short-term impacts on tidal flats (Jarmalavicius et al.,

* Corresponding author.
E-mail address: fxu@sklec.ecnu.edu.cn (F. Xu).

https://doi.org/10.1016/j.geomorph.2025.109977
Received 6 May 2025; Received in revised form 4 August 2025; Accepted 17 August 2025
Available online 20 August 2025

2016; Leonardi et al., 2018), with ongoing debates about their contribution to erosion (Mariotti et al., 2010; Morton and Barras, 2011; Shi et al., 2021) versus accretion (Hache et al., 2021; Pannozzo et al., 2021; Tognin et al., 2021; Xie et al., 2021). However, a ubiquitous atmospheric factor—rainfall—has received much less attention in this context, as it appears neither as intense as storms nor as persistent as tides and waves. Although some studies have examined rainfall's role in sediment redistribution and runoff dynamics (Green and Coco, 2007; Ha et al., 2018; Murphy and Voulgaris, 2006; Voulgaris and Meyers, 2004), most analyses of tidal flat morphodynamics continue to neglect its influence (Fagherazzi et al., 2012; Friedrichs, 2012; Zhou et al., 2022). Lao et al. (2025) notably proposed that rainfall can enhance tidal creek development and sediment transport, but their conceptual model lacked quantification under natural conditions.

Since 2018, a monitoring tower has been established at the Chongming Dongtan tidal flat in the Yangtze River Estuary, China (Fig. 1). The tower is equipped with a camera that provides an aerial view of the upper tidal flat area. This setup offers a unique opportunity to study the influence of rainfall on tidal flat morphodynamics by integrating sediment and flow data from observational frames, meteorological rainfall data, and real-time imagery from the camera. As demonstrated in the subsequent results, we find that rainfall promotes suspended sediment transport and the growth of tidal channel networks across upper tidal flats. These findings provide empirical evidence challenging the conventional focus on prototypical coastal forces, and suggesting that rainfall plays a more considerable role in tidal flat evolution than previously recognized.

2. Materials and methods

2.1. Study area

Chongming Dongtan tidal flat lies at the eastern edge of Chongming Island within the Yangtze River Estuary, which belongs to Shanghai, China. This intertidal wetland spans approximately 170 km^2 and features a complex system of tidal channels (Fig. 1a). The region experiences irregular semi-diurnal tides, with an average tidal range of 2.6 m and an extreme tidal range reaching up to 4.6 m (Shi et al., 2012; Zhu et al., 2016). Under the influence of a subtropical oceanic climate, Chongming Island records a mean annual temperature of 15.2 °C and an average annual precipitation of 1025 mm (Huang et al., 2008). Wind conditions vary throughout the year, with monthly average wind velocities ranging from 3.5 to 4.5 m/s. Typical wave heights measure between 0.1 and 0.3 m, occasionally exceeding 1.0 m during storms (Yang et al., 2008). The surface sediments are predominantly composed of sand and silt (Gorenc et al., 2004; Te Slaa et al., 2013).

2.2. Field measurements

We conducted field measurements in the central area of Chongming Dongtan tidal flat from June 1 to July 31, 2023. A flow-sediment observation system was installed near a primary tidal channel with secondary branches, to collect measurements of flow and sediment dynamics. Notably, the measurement area falls within the field of view of the monitoring tower and is conveniently located near a meteorological station. The measurement area belongs to the upper zone of the tidal flat, located approximately 1.5 m above sea level with a perpendicular distance of about 251 m from the shoreline. The observation system was positioned within the primary tidal channel, 574 m from its entrance. The primary tidal channel has a depth of approximate 1 m; tidal waters overtop the flats when depths exceed 1 m but remain channel-confined below this threshold. The integration of hydrodynamic measurements, video imagery, and meteorological data provides a comprehensive dataset for understanding the evolution and interactions of water, sediment, and geomorphology in the region.

The observation system was equipped with an ALEC INFINITY, a Nortek HR-Profiler and an RBR concerto3-C.T.D. Tu, which measured real-time flow velocity, flow direction, and turbidity. The RBR-TU and

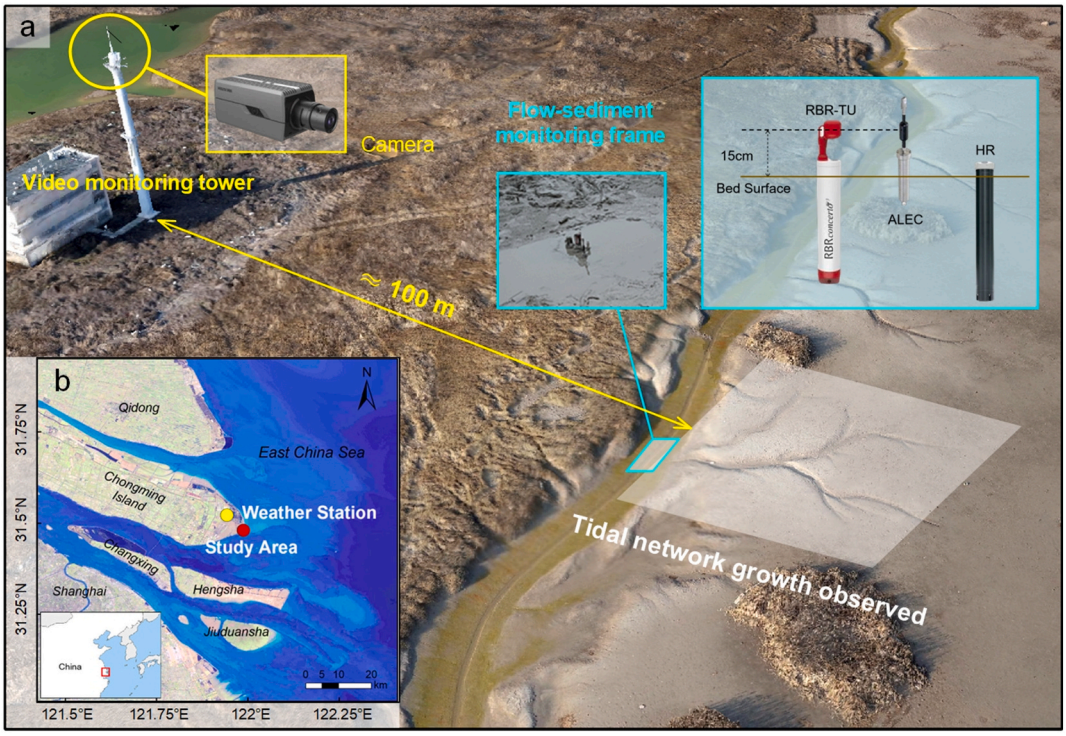

Fig. 1. Study area on the Chongming Dongtan tidal flat in the Yangtze River Estuary, China, where an integrated observation system has been deployed. This system combines a weather station, video monitoring, and a field-based flow-sediment monitoring frame: (a) flow-sediment monitoring instruments, video monitoring tower and the studied secondary channel system; (b) locations of integrated observation system and the weather station.

ALEC sensors were mounted 0.15 m above the bed surface, while the HR sensor was installed closer to the bed. All instruments were securely mounted on dedicated poles designed to minimize the impact of the support structures on the flow (Fig. 1). The burst duration and burst interval for all instruments were set to 60 s and 300 s, respectively, as in previous studies with similar settings (Li et al., 2024; Shi et al., 2017; Xie et al., 2021). The RBR concerto3-C.T.D. Tu operated at 2 Hz, with its optical turbidity sensor accuracy of ±0.125 μmol/m^2/s. The Nortek HR-Profiler operated at 32 MHz with a velocity accuracy of ±0.005 m/s. The ALEC INFINITY sampled at 1 Hz with an accuracy of ±0.01 m/s. During both the deployment and retrieval of the instruments, we collected surface sediment samples near the observation stations. These samples were used to determine the median grain size of the sediments using a Coulter LS-100Q laser particle size analyzer. The Chongming Dongtan Weather Station recorded hourly weather data of July 2023 and June 2023, including wind speed at 10 m above ground and rainfall. The weather station coordinates are 121°56′18.85″E, 31°31′10.60″N, is located only 6.64 km from the observation system. Monthly precipitation data for the Shanghai area from April 2022 to October 2023 were obtained from government environmental bulletins.

We documented the development of the tidal channel system using video data captured by a camera mounted on a 27-m-high tower. The camera recorded continuously during daytime hours at 25 frames per second with a resolution of 3000 × 4000 pixels. The transformation from image coordinates into real-world coordinates was conducted through Direct Linear Transformation (DLT) method (Guo et al., 2020). The mathematical formulas of this transformation can be expressed as (Feng et al., 2024; Hida et al., 2022; Zhan et al., 2019):

$$u\frac{L_1x+L_2y+L_3}{L_7x+L_8y+1} \tag{1}$$

$$v\frac{L_4x+L_5y+L_6}{L_7x+L_8y+1} \tag{2}$$

where *(u,v)* represents image coordinates (in pixels) and *(x,y)* denotes real-world coordinates (in meters). Coefficients L_1-L_8 are calculated through image/real-world coordinates pairs of ground control points (noticeable red marker poles). The outdoor camera system was inevitably subject to minor perturbations from wind, rainfall, and occasional bird interference (Alippi et al., 2010; Žydelis et al., 2019). Measurement errors can also stem from both manual coordinate selection of control points and optical artifacts, such as strong reflections from wet tidal flat surfaces after the ebb tide period. By transforming image coordinates of feature points into real-world view and comparing displacements, we found the mean x-direction error is 0.060 m and the mean y-direction error is −0.038 m, with an average offset of 0.084 m. This implies that the total length of the secondary tidal channel system may be slightly overestimated. However, since the total length spans several tens of meters, this error does not affect the interpretation of the tidal channel's development trend. We employed MATLAB to extract and rectify the video frames and then measured the morphological changes in the tidal channel system.

2.3. Field data processing

The current-induced bed shear stress (τ_c) is evaluated based on the assumption of a logarithmic velocity profile (Whitehouse et al., 2000; Xie et al., 2021):

$$\tau_c = \rho_w u_*^2 \tag{3}$$

$$u(z) = \frac{u_*}{k} ln\left(\frac{z}{z_0}\right) \tag{4}$$

where ρ_w (= 1030 kg/m^3) is the seawater density, u_* (m/s) is the shear velocity, $u(z)$ (m/s) is the current velocity at elevation z (m) above the seabed, κ (= 0.41) is the Von Karman's constant and z_0 (m) is the bed roughness length, which is estimated as the median grain-size of surficial sediment (Colosimo et al., 2020; Lefebvre et al., 2013; Mariotti and Fagherazzi, 2010).

The wave induced bed shear stress (τ_w) takes the form:

$$\tau_w = \frac{1}{2} f_w \rho_w u_b^2 \tag{5}$$

where f_w is the non-dimensional wave friction factor and u_b is the wave orbital velocity (Soulsby and Clarke, 2005):

$$f_w = 0.04\left[\frac{u_b T}{2\pi k_b}\right]^{-0.25} \tag{6}$$

$$u_b = \frac{\pi H}{T sinhkh} \tag{7}$$

where H (m) is the wave height, T (s) is the wave period, $k_b = 2.5d_{50}$ (d_{50} is the median grain size of the bed surface sediment, d_{50}= 14.66 μm), k is the wave number ($\sigma = \sqrt{gk\tanh kh}$, in which $\sigma = 2\pi/T$ is the wave frequency), and h is the water depth. The wave height H and wave period T are calculated using the formulation of Young and Verhagen (1996).

The bed shear stress due to combined Wave-Current Interaction (τ_m) calculated as (Shi et al., 2017; Soulsby and Clarke, 2005):

$$\tau_m = \tau_c\left[1 + 1.2\left(\frac{\tau_w}{\tau_c+\tau_w}\right)^{3.2}\right] \tag{8}$$

The suspended sediment concentration (*SSC*) during the observation period was obtained by converting the turbidity data measured by the RBR-TU (calibration curve is in Supplementary Fig. 1). The suspended sediment flux S_F (kg/m·s) per unit width during the inundation period is calculated as (Nowacki and Ganju, 2019; Sun et al., 2024b):

$$S_F = \frac{\int_0^{T_t} v(t)c(t)h(t)dt}{T_t} \tag{9}$$

where $v(t)$ is the along-channel velocity component (m/s), *c(t)* is the suspended sediment concentration and T_t is the time of the inundation period.

3. Results

3.1. Rainfall-induced morphological changes of tidal flats

The video monitoring system recoded morphodynamic changes in tidal flat morphology from April 2022 to October 2023 (Fig. 2a), when a secondary tidal channel system emerged, branching from the main tidal stream. The total length of the secondary tidal channels is the distance from the branching point off the primary channel to the endpoints of all four secondary channels. This length initially increased rapidly from April to August 2022. After that, the expansion rate gradually slowed. Between January and May 2023, the channel length stabilized at approximately 60 m. Although data gaps exist (August 2022 to December 2022 and April 2023), the growth rate showed a clear deceleration. The channels then resumed growth in June 2023, extending an additional 25 m over the following three months (Fig. 2a; Supplementary Fig. 2).

The secondary growth phase of the channels correlates strongly with rainfall patterns. Meteorological data from a local weather station shows the average monthly rainfall in Shanghai increased markedly from 67.26 mm/month (January–May 2023) to 175.16 mm/month (June–October 2023). This period of intensified precipitation coincided with renewed channel expansion, indicating a potential causal relationship between rainfall and channel development. Fig. 2c further clarifies the relationship between monthly secondary channel extension length and precipitation. Beginning in January 2023, a pronounced positive

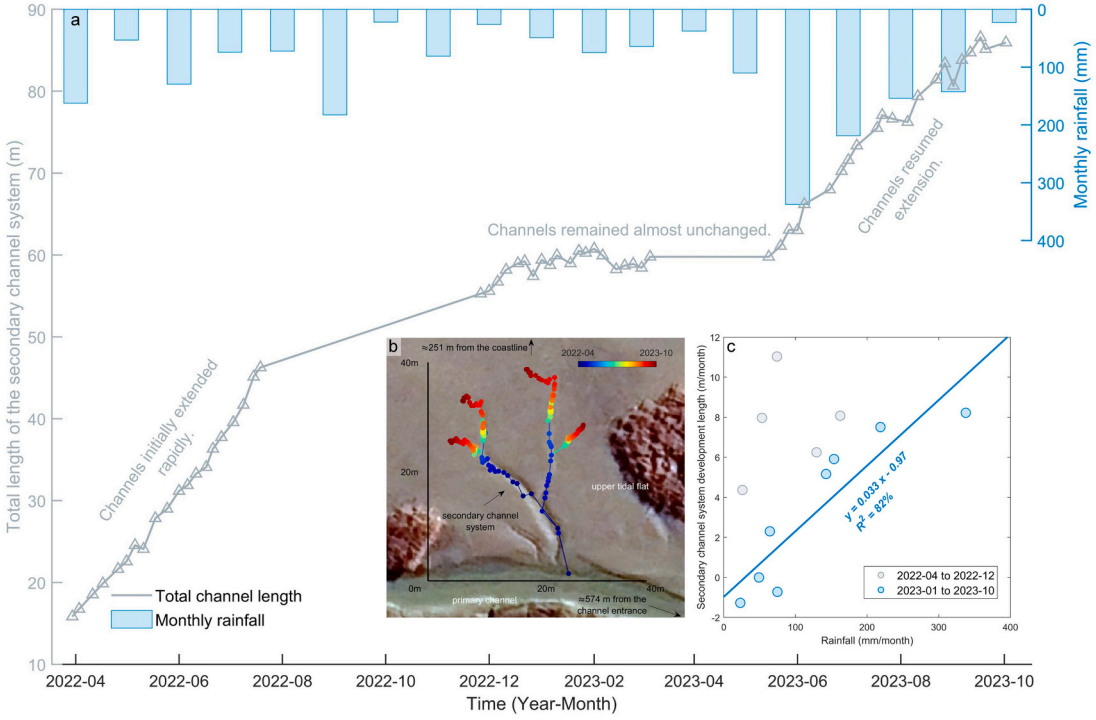

Fig. 2. The development process of the secondary tidal channel system and its correlation with rainfall: (a) The total length of the secondary tidal channel system from April 2022 to October 2023; (b) Changes in the endpoint positions of each branch in the secondary tidal channel system from the true top-down view; (c) Correlation between the monthly extension length of the secondary channel system and rainfall.

correlation emerges, indicating that rainfall has become the primary driver of channel growth. In contrast, data from before 2023 lie predominantly above the regression line, revealing a weaker correspondence with rainfall. This temporal shift reflects changing geomorphic controls: in 2022, the secondary channels occupied lower-elevation flats subject to frequent tidal inundation, and headward erosion induced by tidal action governed their expansion. As channel heads migrated onto higher-elevation tidal flats—where inundation frequency diminished markedly—the influence of tides waned and rainfall-driven incision assumed primacy in controlling channel elongation. The absence of severe storm events in the observation area from June to October 2023 (Supplementary Fig. 3) eliminates storm impacts as a primary driver of the observed channel growth. However, questions remain about the influence of increased winds, elevated wave conditions, and rainfall-induced flow inputs during wetter months. These factors require additional investigation to determine their relative contributions to channel development.

3.2. Impacts of rainfall on flow patterns

We monitored hydrodynamic conditions across 56 tidal cycles over two months between June and August 2023. The remaining tidal cycles were not captured because the water did not submerge the study area. During the observed inundation periods, the recorded water depths ranged from 0.2 m to 1.5 m, while flow velocities reached up to 1 m/s. These observations included 42 inundation cycles under rain-free conditions (Fig. 3a–f) and 14 inundation cycles during rainy conditions (Fig. 3g–h). Most rainfall events covered the entire inundation period, with an average rainfall intensity of 2.58 mm/h and a maximum intensity reaching 20 mm/h. To facilitate interpretation, we sorted the data by maximum water depth, which reflects the tidal range. The full-time data series of the observations is provided in Supplementary Fig. 3.

Under rain-free conditions, tidal currents exhibit clear flood and ebb flow patterns corresponding with the rise and fall of the tide (represented by the colour of dots in Fig. 3a–f). When the tidal range is small (e.g., N1-N21), high flow velocities typically occur near the beginning and end of the inundation period, coinciding with periods of rapid water-level change. As the tidal range increases, water overtops the flats at high tide (e.g., N29-N42), resulting in two additional flow velocity peaks near the high-water phase (one at flood tide and one at ebb tide). This transition reflects variations in ebb and flood dominance under different tidal conditions. Specifically, for smaller tidal ranges, where depths are small, flood velocities exceed ebb velocities (e.g., N1-N21), resembling the typical dynamics of tidal flats(Ge et al., 2021; Wang et al., 2020; Xie et al., 2018).In contrast, for larger tidal ranges (e.g., N29-N42), water overflows across tidal flats inducing a shift toward ebb dominance as water drains back into the channels (Fig. 3e–f). These observed patterns are consistent with established understandings of tidal flat-channel hydrodynamics.

During rainy conditions, the flow field does not show regular flood and ebb patterns as in rain-free conditions (Fig. 3g-h). A notable difference is that the flow tends toward ebb dominant in nearly all observed rainy inundation cycles (e.g., compare N1-N7 with R1-R7). Even under large tidal ranges (e.g., R13), rainfall can reverse the flow direction to ebb-directed during the flood phase. We attribute this ebb-dominated trend to the rainwater draining from the tidal flats into the channel. In addition, the rainfall affects flow velocity magnitude. For example, heavy rainfall (e.g., >10 mm/h) during neap tides generated large ebb flow velocities comparable to those observed during rainy-free spring tides (e.g., compare N40–N41 with R5–R6). This result further suggests that the distortion of flow patterns in rainy days can be as significant as the effects of tidal forcing.

No strong winds or extreme typhoon events occurred during the observation period. The average wind speed throughout the observation period was less than 5 m/s, with easterly and southerly being the prevailing wind directions (Supplementary Fig. 3). Only during the N33, R7, N23, R10 periods wind speeds reach 10 m/s. Given the generally low wind speeds during this period, the impact of wind on flow velocity was small (Supplementary Fig. 4). This can be illustrated through two comparative examples: although wind speeds differed by 5 m/s between

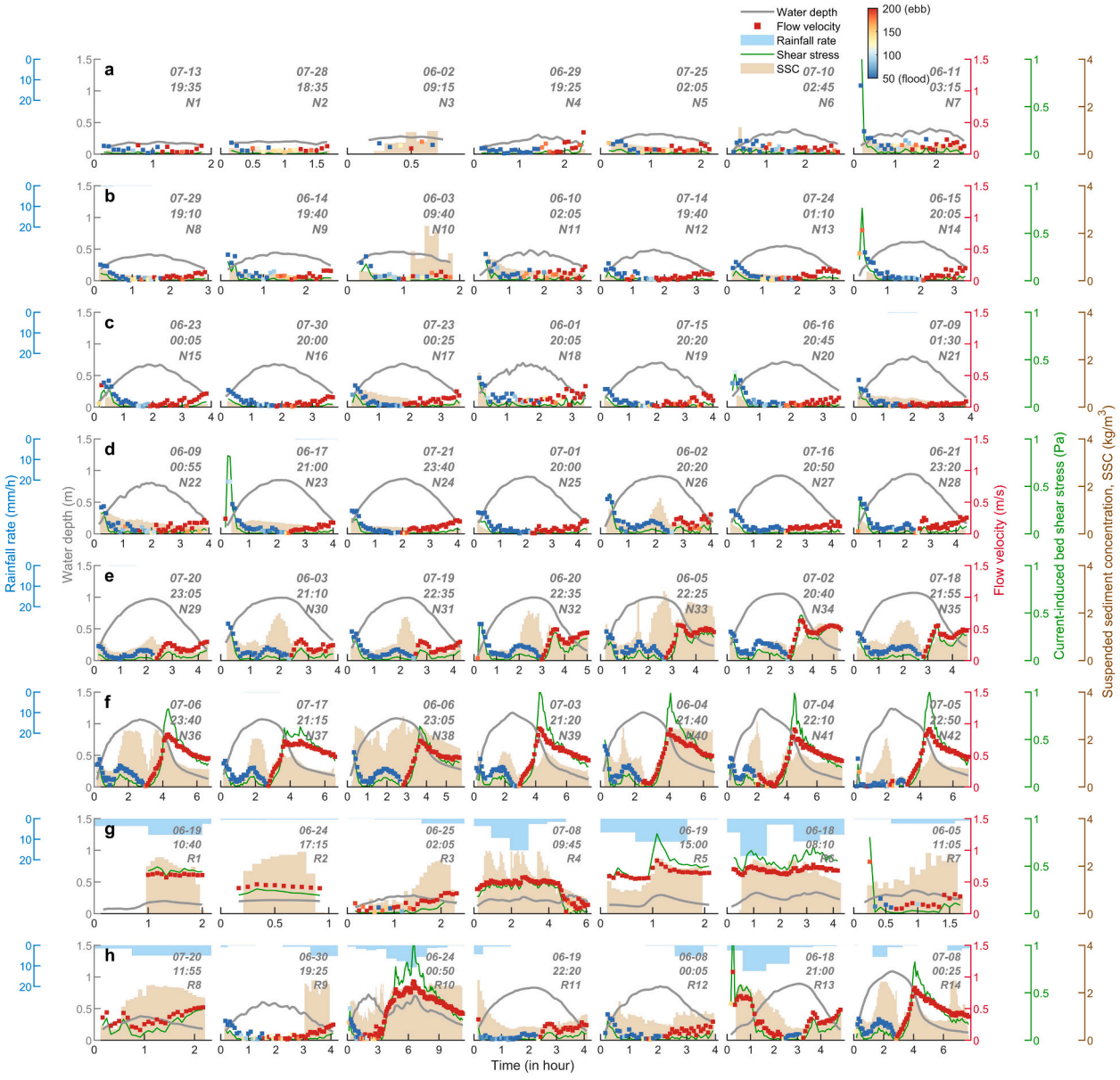

Fig. 3. Water depth (gray lines), flow velocity (dots), current-induced bed shear stress (green lines), and suspended sediment concentration (brown bars) recorded during all tidal inundation periods, along with the corresponding rainfall rate (blue bars). The colour of the velocity points indicates the direction of flow, with red representing ebb tide and blue representing flood tide. The inundation periods are arranged in ascending order of maximum water depth rather than chronological order, and the beginning and times of each inundation period are noted with the inundation period number. The beginning and ending times for each inundation period are also in Supplementary Table 1.

N23 and N25, which exhibited similar tidal patterns, their flow velocity distributions were nearly identical; the average wind speed of N33 was 6 m/s higher than that of N39, but the flow velocity of N33 was even lower than that of N39. Therefore, we attribute the significant variations in tidal flow velocity observed during rainy conditions to the additional precipitation input.

3.3. *Impacts of rainfall on suspended sediment transport*

There is a clear positive correlation between overall SSC and the strength of tidal forces during rain-free periods (brown bars in Fig. 3a-f). Specifically, large SSC values are mostly observed during spring tides, particularly when the maximum water depth exceeds approximately 1 m (e.g., N29-N42, see Fig. 3e-f). SSC time series do not strictly follow the fluctuations in flow velocity or current-induced bed shear stress, as suspended sediment is not sourced exclusively from local scour. However, the SSC time series shows recognizable patterns and commonalities for similar tidal conditions. For example, during spring tides (e.g., N30-N32, etc.), SSC peaks coincide with higher water levels. On the other hand, during rainy days, high SSC values are observed even under low tidal range (Fig. 3g-h). Furthermore, the timing of elevated SSC aligns closely with the occurrence of rainfall events (e.g., R1, R3, R6, R13 and R14). These observations suggest that rainfall is a significant meteorological factor contributing to increased SSC.

To investigate how rainfall events enhance SSC, we averaged the current-induced bed shear stress, rainfall rate, and SSC for each inundation cycle (Fig. 4). In the absence of rainfall, we identified a threshold maximum water depth of approximately 1 m (see gray triangles and regression lines). Below this depth, bed shear stress remains low and exhibits minimal variation, as indicated by the low R^2 ($\approx$ 4%) in the linear regression. However, shear stress increases sharply when the maximum water depths exceed this threshold. Here, we consider the 1-m

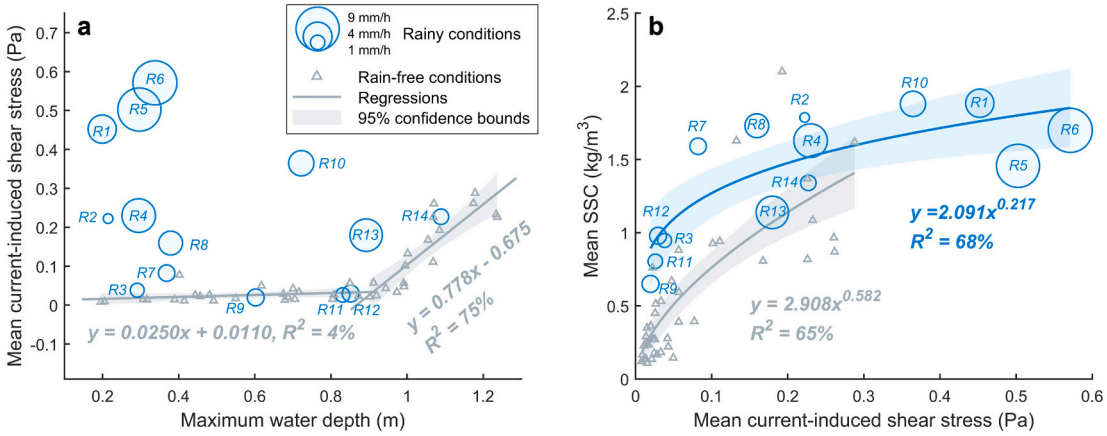

Fig. 4. Variations in bed shear stress and suspended sediment concentration (SSC) during rainy and rain-free periods. (a) Relationship between the mean current-induced shear stress and maximum water depth (representing tidal range); (b) Relationship between the mean SSC and mean current-induced shear stress. Gray triangles and blue circles represent rainy and rain-free conditions, respectively. The size of the circles corresponds to the rainfall rate. The blue and gray lines indicate the regressions of the respective data, with the shaded bands representing 95 % confidence intervals.

maximum water depth as the point at which tidal flow overtops the tidal channel banks. As the water level rises above this depth, the tidal flow rapidly spreads across the tidal flats, resulting in a substantial increase in tidal volume and, consequently, higher overall erosion forces (current-induced bed shear stress).

However, rainfall disrupts this typical variation pattern (blue circles in Fig. 4a). Under low rainfall conditions, the mean current-induced bed shear stress variation exhibits patterns similar to rain-free conditions (e.g., R3, R9, R11, R2, and R14). However, intense rainfall events generate significantly higher current-induced bed shear stress (e.g., R1, R5, R6, and R10). We further tested the relationships between mean current-induced bed shear stress and mean SSC separately for rainy and rain-free conditions (Fig. 4b). Both relationships are well-fitted by power-law functions (gray and blue curves). However, the mean SSC values during rainfall events consistently exceed those during rain-free periods, even under equivalent mean shear stress conditions. In addition, the rate at which SSC changes with shear stress during rainfall reduces under rainy conditions (see the different slopes of the blue and gray curves). These differences suggest rainfall contributes additional suspended sediment input from tidal flats through runoff.

To quantify the contribution of rainfall events to sediment transport, we calculated the net sediment flux during each tidal inundation period (Fig. 5). Under rain-free conditions, when tidal water did not overtop the flats ($h_{max} < 1$ m), the system exhibited a slight flood dominance with a net sediment flux of less than 0.05 kg/m·s (thin-outlined gray bars). When tidal water overtopped the flats ($h_{max} > 1$ m), the transport pattern shifted predominantly to ebb-directed (thick-outlined gray bars). During rainfall events, the transport pattern consistently displayed strong ebb dominance (blue bars). Notably, most rainfall events coincided with periods when tidal water did not overtop the flats—conditions that typically produce flood-dominated transport (represented by the predominantly thin-outlined blue bars). This observation suggests that rainfall was the primary driver of ebb dominance. Furthermore, statistical analysis of all inundation periods (irrespective of tidal overtopping) demonstrates, although rainfall events accounted for 25 % of the total observed inundation periods (1/3 of the rain-free periods), they contributed 62 % of the cumulative net sediment transport (about 1.5 times the rain-free periods). This result suggests

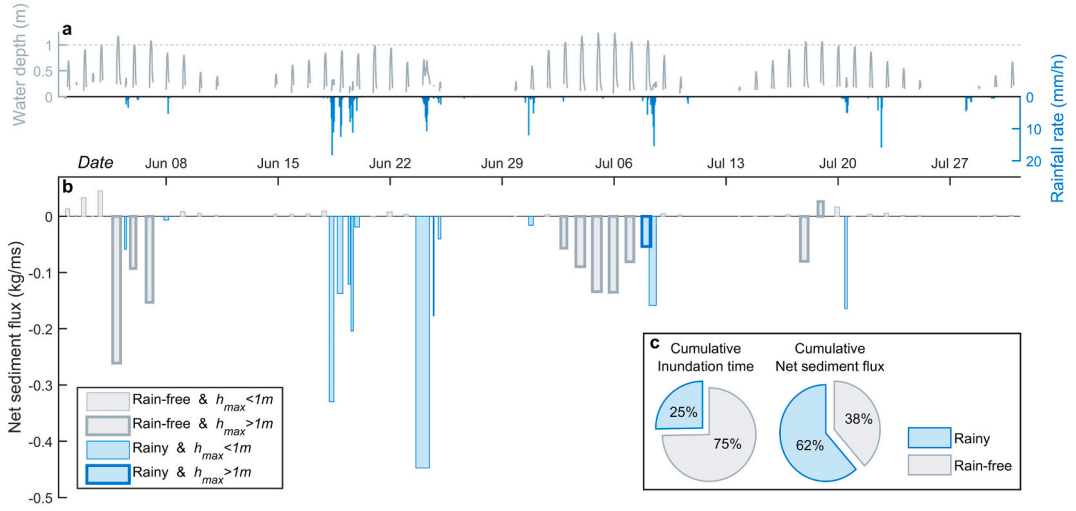

Fig. 5. (a) Water depth and rainfall time series; (b) Net sediment flux for each tidal inundation cycle; (c) The pie chart which shows the proportion of rainy and rain-free conditions in terms of the cumulative inundation time and net sediment flux. Gray and blue bars represent rainy and rain-free conditions, respectively. The width of the bars indicates the duration of inundation. A thick outline around a bar indicates that the maximum water depth (h_{max}) during that inundation cycle exceeded 1 m, suggesting that the flow overtopped the tidal channel bank. The pie chart in the lower right corner shows the proportion of rainy and rain-free conditions in terms of the cumulative inundation time and net sediment flux.

that at the upper flat(e.g.1.5 m above sea level with tidal range around 2.6 m in this study)rainfall can reach to nearly 5 times more efficient than tidal forcing in driving net sediment transport. Our conclusions are valid across dry and rainy seasons and over the spatial extent of the upper tidal flat, approximately 10^3 m^2 (the typical coverage area of the secondary channel system). We consider the spatial effectiveness of rainfall-induced processes is also influenced by the size of the tidal flat's catchment area, with larger tidal flats experiencing more intense rainfall showing more pronounced effects.

4. Discussion

4.1. Mechanisms of rainfall-driven sediment dynamics

Under rain-free conditions, the overflow of tidal water across channel banks serves as a critical threshold for hydrodynamic regime shifts in tidal channels. When water overtops the banks, it expands the effective drainage area by incorporating adjacent tidal flats, thereby increasing discharge through the channel. This enhanced discharge results in nonlinear increases in bed shear stress and sediment resuspension (Fig. 4). Although tidal flows are amplified during both flood and ebb tides, the system predominantly exhibits an ebb-dominated sediment transport pattern (Fig. 5). This asymmetry arises from the higher bed resistance of tidal flats compared to the main channel, which reduces flow velocities over the flats. During the flood, this frictional differential leads to higher water levels in the channel as the flow struggles to spread across the tidal flat surface(Fagherazzi et al., 2008). Conversely, during the ebb, the delayed drainage from the tidal flats (due to friction-induced lag) forces the flow to be confined to a smaller effective depth. As a result, the ebb phase experiences higher bed shear stresses and sediment transport capacity than the flood phase (e.g., Fig. 3f).

The above-mentioned mechanism extends to rainfall scenarios, as rainwater facilitates hydraulic connectivity between channels and adjacent tidal flats through surface runoff. This connection operates independently of tidal pumping overflow and thus exclusively contributes to ebb-directed sediment transport. At the onset of the flood tide under low water levels, rainfall-induced runoff can significantly alter flow direction and increase bed shear stress, thereby enhancing local sediment suspension (e.g., R11 and R13 in Fig. 3). When rainfall occurs during high-water stages (e.g., R14) or ebb tides (e.g., R7, R12, and R14), it does not substantially increase flow velocity or shear stress, but suspended sediment concentrations (SSC) still rise. This suggests the additional sediment originates from rainwater scouring sediments off the tidal flats. In particular, during neap tide conditions when tidal inundation remains subcritical (e.g., R1-R7 in Fig. 3g), rainfall-generated runoff converges directly into tidal channels at shallow water depths. The concentrated discharge under these low-stage conditions generates disproportionately high bed shear stresses compared to tidal flows (Fig. 4a). Furthermore, suspended sediment concentrations under rainfall conditions consistently exceed values observed under equivalent shear stress conditions without rainfall. We consider this enhancement stems from two mechanisms: (1) raindrop impact energy destabilizes surface sediments on exposed tidal flats, increasing their erodibility (Ha et al., 2018; Kleinhans et al., 2009; Tolhurst et al., 2006), and (2) precipitation can influence broader supratidal areas than those typically inundated during high tides, creating more extensive contributing areas for runoff convergence (Kim et al., 2021; Murphy and Voulgaris, 2006; Xin et al., 2017). This mechanism resonates with observations from seasonal rainfall pulses in Amazonian mangroves (Cardenas et al., 2022) and on the west coast of Korea (Choi and Jo, 2015), where similar hydraulic connectivity significantly influences channel elongation and sediment transport dynamics. Rainfall may also promote sediment mobilization by triggering biological processes (Alberti et al., 2007; Meynecke et al., 2006). Rainfall can stimulate the activity of benthic organisms such as crabs, including burrowing, feeding, and migrating behaviors, which disturb sediments and contribute to creek formation (Hewitt et al., 2022; Luppi et al., 2013; Orvain et al., 2014). Rainfall may also disrupt and dissolve biofilms, rendering surface sediments more susceptible to tidal erosion (Chen & Torres, 2018; Tolhurst et al., 2006).

4.2. Implications for tidal flat morphodynamics and resilience

Tidal forcing serves as the primary driver of tidal creek extension, primarily through headward erosion processes (Chirol et al., 2018; Novakowski et al., 2004; Rinaldo et al., 1999). Wave action typically plays a counteracting role by redistributing sediments and smoothing creek morphology (de Vet et al., 2018; Sun et al., 2024c). Fluvial inputs can also facilitate channel network expansion by introducing hydrodynamic energy and delivering sediment that may be deposited within the channels (Li et al., 2025; Wang et al., 2020). On the other hand, this study shows that rainfall is also a significant contributor to tidal creek extension on upper tidal flats. Our results underscore the underestimated role of rainfall in driving tidal flat evolution. Specifically, rainfall effectively integrates upper tidal flats into active sediment cycles. The rainwater-driven runoff creates ephemeral drainage networks that enable hydrodynamic forces to access and modify previously isolated supratidal areas. This process extends the spatial domain of morphodynamic processes beyond conventional tidal inundation limits. In addition, the observed ebb-dominated sediment transport does not imply simple offshore export but likely drives complex redistribution pathways. For instance, rainfall-mobilized sediments may be temporarily deposited along tidal flat margins, intercepted by adjacent channel networks, or recirculated landward during subsequent flood tides through newly formed drainage conduits. This intricate sediment routing increases connectivity across the tidal flat system and potentially reinforces morphodynamic feedbacks that govern long-term landscape evolution.

In addition, rainfall-induced sediment transport could alter the carbon dynamics of tidal flats (Chen and Lee, 2022; Sasmito et al., 2020; Zhu and Olsen, 2014). During rainfall events, intensified hydrodynamic forces promote larger sediment erosion, exporting organic-rich sediment and releasing previously sequestered carbon into the water column(Pan et al., 2025; Rios-Yunes et al., 2023; Sakamaki and Nishimura, 2007). Erosion further exposes protected anaerobic zones to oxygen, accelerating organic carbon mineralization and possibly resulting in elevated carbon dioxide emissions (Mckew et al., 2013; Spivak et al., 2019; Steinmuller et al., 2019). Therefore, omitting rainfall effects in carbon flux evaluations could lead to biased assessments of tidal flats, potentially misclassifying them as stable carbon sinks when they may transition into carbon sources under increased rainfall conditions (Mok et al., 2019; Sakamaki and Nishimura, 2006).

The implications extend regarding the resilience of tidal flats under climate change scenarios. Intensified rainfall regimes may amplify erosion risks, even in sheltered, low-energy settings (Seneviratne et al., 2021). Rainfall-driven channel growth enhances drainage efficiency, potentially accelerating marsh degradation through creek network expansion—a feedback loop previously attributed mainly to sea-level rise (Kirwan and Megonigal, 2013). For example, in the Wadden Sea, a UNESCO World Heritage site, increased autumn rainfall could destabilize historically stable upper tidal flats, complicating existing management strategies that primarily target tidal and wave energy (Baptist et al., 2019). On the other hand, in regions experiencing decreased rainfall, such as parts of the Australian east coast (Speer et al., 2011), sediment transport and deposition onto tidal flats might be enhanced. However, these hypotheses demand further detailed investigation to validate the nuanced interactions between rainfall variability, sediment dynamics, and tidal flat resilience under changing climatic conditions (Ranasinghe et al., 1999).

4.3. Limitations and future perspectives

While synchronized video and flow-sediment records provide direct evidence of rainfall-mediated transport mechanisms, several methodological limitations merit attention. Due to instrumental constraints, we only analyzed the morphological changes of the secondary tidal channel system and did not conduct a comprehensive three-dimensional reconstruction. The camera cannot operate at night, resulting in the omission of spring tide overbank flows in the study area. This limitation impedes fully characterizing hydrodynamic-morphodynamic interactions during these high-energy tidal surges. Additionally, the single measurement point restricts detailed mapping of spatial heterogeneity in sediment transport patterns across the tidal flat.

Addressing these observational gaps would benefit from coordinated advancements in monitoring techniques and numerical modeling approaches. Multi-angle photogrammetric systems with LiDAR sensors offers a promising solution to reconstructing three-dimensional topography changes. Conducting repeated terrestrial laser scanning before and after rainfall events would significantly expand the research scope to bare flats and vegetated zones and enable a more comprehensive understanding of rainfall-induced geomorphological changes across entire tidal flat (Xie et al., 2017). Concurrently, incorporating more detailed representations of rainfall processes could improve the prediction of morphodynamic models, such as distinguishing the differences in morphodynamics between dry and wet seasons (Engelbrecht and Landman, 2016; Hossain et al., 2014; Sumner et al., 2001). This might include modules for raindrop kinetic energy to capture sediment destabilization and precipitation-driven runoff algorithms better to quantify contributions from supratidal areas. To effectively implement these improvements, laboratory experiments could combine rainfall simulators with tidal flat physical models to calibrate relevant empirical parameters (e.g., threshold shear stress for sediment erosion). In addition, field efforts could deploy distributed sensor networks across tidal flat elevation gradients to monitor spatial variations in sediment dynamics and improve model validation.

5. Conclusions

This study investigates the influence of rainfall on tidal flat morphology by integrating hydrodynamic sediment data, meteorological precipitation records, and visual observations. We provide clear observational evidence that rainfall events are associated with high flow velocities, increased suspended sediment concentrations, and more pronounced topographical changes than rain-free conditions. Specifically, while rainfall events account for only 25 % of the observed tidal inundation periods, they contribute to 62 % of the cumulative net sediment transport. This increased transport is primarily driven by runoff from the upper tidal flats into the tidal channels, enhancing scouring forces and promoting sediment transport in the ebb direction. These findings suggest re-evaluating the prevailing research focus on tidal, wave, and storm surge dynamics, underscoring the need to incorporate rainfall-driven processes into frameworks for analyzing coastal morphodynamics.

CRediT authorship contribution statement

Shang Yu: Writing – original draft, Visualization, Methodology, Investigation, Formal analysis, Data curation, Conceptualization. **Fan Xu:** Writing – original draft, Visualization, Supervision, Software, Methodology, Funding acquisition, Conceptualization. **Weiming Xie:** Validation, Methodology, Funding acquisition, Formal analysis. **Xianye Wang:** Resources, Methodology, Funding acquisition. **Chunyan Zhu:** Validation, Funding acquisition. **Qing Yuan:** Software, Resources, Project administration. **Haisheng Yu:** Software, Investigation. **Zhonghao Zhao:** Methodology, Investigation. **Yijie Zhang:** Investigation, Data curation. **Zhengbing Wang:** Writing – review & editing, Methodology, Investigation. **Giovanni Coco:** Writing – review & editing, Methodology, Formal analysis. **Qing He:** Writing – review & editing, Supervision, Resources, Project administration, Funding acquisition, Formal analysis.

Declaration of competing interest

The authors declare that they have no known competing financial interests or personal relationships that could have appeared to influence the work reported in this paper.

Acknowledgments

This research was supported by the National Natural Science Foundation of China (No. 42376168) and the National Key Research and Development Program of China (Nos. 2024YFE0103100, 2022YFA1004401, and 2023YFC3208500). Financial support from the National Natural Science Foundation of China (Nos. U24A201762, 42276217, 42476215, and 42206169) is also acknowledged. We thank the Shanghai Chongming Dongtan National Nature Reserve for their support with field observations.

Appendix A. Supplementary data

Supplementary data to this article can be found online at https://doi.org/10.1016/j.geomorph.2025.109977.

Data availability

Data will be made available on request.

References

Alberti, J., Montemayor, D., Álvarez, F., Méndez Casariego, A., Luppi, T., Canepuccia, A., et al., 2007. Changes in rainfall pattern affect crab herbivory rates in a SW Atlantic salt marsh. J. Exp. Mar. Biol. Ecol. 353 (1), 126–133. https://doi.org/10.1016/j.jembe.2007.09.007.

Alippi, C., Boracchi, G., Camplani, R., Roveri, M., 2010. Detecting external disturbances on the camera lens in wireless multimedia sensor networks. IEEE Trans. Instrum. Meas. 59, 2982–2990. https://doi.org/10.1109/TIM.2010.2047129.

Allen, J.R.L., 2000. Morphodynamics of Holocene salt marshes: a review sketch from the Atlantic and Southern North Sea coasts of Europe. Quat. Sci. Rev. 19 (12), 1155–1231. https://doi.org/10.1016/S0277-3791(99)00034-7.

Andersen, T.J., Pejrup, M., Nielsen, A.A., 2006. Long-term and high-resolution measurements of bed level changes in a temperate, microtidal coastal lagoon. Mar. Geol. 226 (1–2), 115–125. https://doi.org/10.1016/j.margeo.2005.09.016.

Baptist, M.J., van der Wal, J.T., Folmer, E.O., Gräwe, U., Elschot, K., 2019. An ecotope map of the trilateral Wadden Sea. J. Sea Res. 152, 101761. https://doi.org/10.1016/j.seares.2019.05.003.

Belliard, J.P., Silinski, A., Meire, D., Kolokythas, G., Levy, Y., Van Braeckel, A., et al., 2019. High-resolution bed level changes in relation to tidal and wave forcing on a narrow fringing macrotidal flat: Bridging intra-tidal, daily and seasonal sediment dynamics. Mar. Geol. 412, 123–138. https://doi.org/10.1016/j.margeo.2019.03.001.

Cardenas, S.M.M., Cohen, M.C.L., Ruiz, D.P.C., Souza, A.V., Gomez-Neita S., Juan, Pessenda, L.C.R., Culligan, N., 2022. Death and regeneration of an Amazonian mangrove forest by anthropic and natural forces. Remote Sens. 14 (24), 6197. https://doi.org/10.3390/rs14246197.

Chen, Z.L., Lee, S.Y., 2022. Sediment carbon sequestration and sources in peri-urban tidal flats and adjacent wetlands in a megacity. Mar. Pollut. Bull. 185. https://doi.org/10.1016/j.marpolbul.2022.114368.

Chen, S., Torres, R., 2018. Biogeochemical characteristics and fluxes of suspended particulate organic matter in response to low-tide rainfall. Limnol. Oceanogr. 63, S307–S323. https://doi.org/10.1002/lno.10741.

Chirol, C., Haigh, I.D., Pontee, N., Thompson, C.E., Gallop, S.L., 2018. Parametrizing tidal creek morphology in mature saltmarshes using semi-automated extraction from lidar. Remote Sens. Environ. 209, 291–311. https://doi.org/10.1016/j.rse.2017.11.012.

Choi, K., Jo, J.H., 2015. Morphodynamics of tidal channels in the open coast macrotidal flat, Southern Ganghwa Island in Gyeonggi Bay, West Coast of Korea. J. Sediment. Res. 85 (6), 582–595. https://doi.org/10.2110/jsr.2015.44.

Coco, G., Zhou, Z., van Maanen, B., Olabarrieta, M., Tinoco, R., Townend, I., 2013. Morphodynamics of tidal networks: advances and challenges. Mar. Geol. https://doi.org/10.1016/j.margeo.2013.08.005.

Colosimo, I., de Vet, P.L.M., van Maren, D.S., Reniers, A.J.H.M., Winterwerp, J.C., van Prooijen, B.C., 2020. The impact of wind on flow and sediment transport over intertidal flats. J Mar Sci Eng 8 (11), 1–26. https://doi.org/10.3390/jmse8110910.

de Vet, P.L.M., van Prooijen, B.C., Schrijvershof, R.A., van der Werf, J.J., Ysebaert, T., Schrijver, M.C., Wang, Z.B., 2018. The importance of combined tidal and meteorological forces for the flow and sediment transport on intertidal shoals. J. Geophys. Res. Earth 123 (10), 2464–2480. https://doi.org/10.1029/2018JF004605.

Engelbrecht, C.J., Landman, W.A., 2016. Interannual variability of seasonal rainfall over the Cape south coast of South Africa and synoptic type association. Clim. Dyn. 47 (1–2), 295–313. https://doi.org/10.1007/s00382-015-2836-2.

Fagherazzi, S., Priestas, A.M., 2010. Sediments and water fluxes in a muddy coastline: interplay between waves and tidal channel hydrodynamics. Earth Surf. Process. Landf. 35 (3), 284–293. https://doi.org/10.1002/esp.1909.

Fagherazzi, S., Wiberg, P.L., 2009. Importance of wind conditions, fetch, and water levels on wave-generated shear stresses in shallow intertidal basins. J. Geophys. Res. Earth Surf. 114 (3). https://doi.org/10.1029/2008JF001139.

Fagherazzi, Sergio, Carniello, L., D'alpaos, L., Defina, A., 2006. Critical bifurcation of shallow microtidal landforms in tidal flats and salt marshes. Proc. Natl. Acad. Sci. USA 103. www.pnas.orgcgidoi10.1073pnas.0508379103.

Fagherazzi, Sergio, Hannion, M., D'Odorico, P., 2008. Geomorphic structure of tidal hydrodynamics in salt marsh creeks. Water Resour. Res. 44 (2). https://doi.org/10.1029/2007WR006289.

Fagherazzi, Sergio, Kirwan, M.L., Mudd, S.M., Guntenspergen, G.R., Temmerman, S., D'Alpaos, A., et al., 2012. Numerical models of salt marsh evolution: ecological, geomorphic, and climatic factors. Rev. Geophys. 50 (1). https://doi.org/10.1029/2011RG000359.

Feng, H., Chen, F., Heng, W., 2024. Reconstruction of the motion of traffic accident vehicle in the vehicle-mounted video based on direct linear transform. J. Adv. Transp. 2024 (1). https://doi.org/10.1155/2024/5793435.

Fivash, G.S., Temmerman, S., Kleinhans, M.G., Heuner, M., van der Heide, T., Bouma, T. J., 2023. Early indicators of tidal ecosystem shifts in estuaries. Nat. Commun. 14 (1). https://doi.org/10.1038/s41467-023-37444-6.

Friedrichs, C.T., 2012. Tidal flat morphodynamics: a synthesis. In: Treatise on Estuarine and Coastal Science, vol. 3. Elsevier Inc, pp. 137–170. https://doi.org/10.1016/B978-0-12-374711-2.00307-7.

Friedrichs, C.T., Aubrey, D.G., 2011. Uniform Bottom Shear Stress and Equilibrium Hyposometry of Intertidal Flats, pp. 405–429. https://doi.org/10.1029/ce050p0405.

Friedrichs, C.T., Perry, J.E., 2001. Tidal Salt Marsh Morphodynamics: A Synthesis. J. Coast. Res. 7–37. http://www.jstor.org/stable/25736162.

Ge, J., Yi, J., Zhang, J., Wang, X., Chen, C., Yuan, L., et al., 2021. Impact of vegetation on lateral exchanges in a salt marsh-tidal creek system. J. Geophys. Res. Earth 126 (8). https://doi.org/10.1029/2020JF005856.

Gong, Z., Jin, C., Zhang, C., Zhou, Z., Zhang, Q., Li, H., 2017. Temporal and spatial morphological variations along a cross-shore intertidal profile, Jiangsu, China. Cont. Shelf Res. 144, 1–9. https://doi.org/10.1016/j.csr.2017.06.009.

Gorenc, S., Kostaschuk, R., Chen, Z., 2004. Spatial variations in heavy metals on tidal flats in the Yangtze Estuary, China. Environ. Geol. 45 (8), 1101–1108. https://doi.org/10.1007/s00254-004-0968-5.

Green, M.O., Coco, G., 2007. Sediment transport on an estuarine intertidal flat: measurements and conceptual model of waves, rainfall and exchanges with a tidal creek. Estuar. Coast. Shelf Sci. 72 (4), 553–569. https://doi.org/10.1016/j.ecss.2006.11.006.

Green, Malcolm O., Coco, G., 2014. Review of wave-driven sediment resuspension and transport in estuaries. Rev. Geophys. https://doi.org/10.1002/2013RG000437.

Guo, J., Shi, L., Pan, S., Ye, Q., Cheng, W., Chang, Y., Chen, S., 2020. Monitoring and evaluation of sand nourishments on an embayed beach exposed to frequent storms in eastern China. Ocean Coast. Manag. 195. https://doi.org/10.1016/j.ocecoaman.2020.105284.

Ha, H.J., Kim, H., Noh, J., Ha, H.K., Khim, J.S., 2018. Rainfall effects on the erodibility of sediment and microphytobenthos in the intertidal flat. Environ. Pollut. 242, 2051–2058. https://doi.org/10.1016/j.envpol.2018.06.079.

Hache, I., Karius, V., von Eynatten, H., 2021. Storm surge induced sediment accumulation on marsh islands in the southeastern North Sea: implications for coastal protection. Estuar. Coast. Shelf Sci. 263. https://doi.org/10.1016/j.ecss.2021.107629.

Hewitt, D.E., Niella, Y., Johnson, D.D., Suthers, I.M., Taylor, M.D., 2022. Crabs go with the flow: declining conductivity and cooler temperatures trigger spawning migrations for female giant mud crabs (Scylla serrata) in subtropical estuaries. Estuar. Coasts 45 (7), 2166–2180. https://doi.org/10.1007/s12237-022-01061-1.

Hida, T., Okada, T., Matsumoto, T., 2022. Work postural ergonomic assessment using two-dimensional joint coordinates. J. Adv. Mech. Des. Syst. Manuf. 16. https://doi.org/10.1299/jamdsm.2022jamdsm0055.

Hossain, M.S., Roy, K., Datta, D.K., 2014. Spatial and temporal variability of rainfall over the south-west coast of Bangladesh. Climate 2 (2), 28–46. https://doi.org/10.3390/cli2020028.

Hu, Z., Wang, Z.B., Zitman, T.J., Stive, M.J.F., Bouma, T.J., 2015. Predicting long-term and short-term tidal flat morphodynamics using a dynamic equilibrium theory. J. Geophys. Res. Earth 120 (9), 1803–1823. https://doi.org/10.1002/2015JF003486.

Huang, B., Ouyang, Z., Zheng, H., Zhang, H., Wang, X., 2008. Construction of an eco-island: a case study of Chongming Island, China. Ocean Coast. Manag. 51 (8–9), 575–588. https://doi.org/10.1016/j.ocecoaman.2008.06.007.

Jarmalavicius, D., Šmatas, V., Stankunavicius, G., Pupienis, D., Žilinskas, G., 2016. Factors controlling coastal erosion during storm events. J. Coast. Res. 1, 1112–1116. Coastal Education Research Foundation Inc. https://doi.org/10.2112/SI75-223.1.

Kim, D., Jo, J., Choi, K., 2021. Role of rainfall-induced runoff discharge and human disturbance on the morphodynamics and sedimentation in the semienclosed macrotidal flats (Shinsi tidal flats, Korea). Mar. Geol. 438. https://doi.org/10.1016/j.margeo.2021.106522.

Kirwan, M.L., Megonigal, J.P., 2013. Tidal wetland stability in the face of human impacts and sea-level rise. Nature 504 (7478), 53–60. https://doi.org/10.1038/nature12856.

Kleinhans, M.G., Schuurman, F., Bakx, W., Markies, H., 2009. Meandering channel dynamics in highly cohesive sediment on an intertidal mud flat in the Westerschelde estuary, the Netherlands. Geomorphology 105 (3–4), 261–276. https://doi.org/10.1016/j.geomorph.2008.10.005.

Lao, C., Zhao, L., Zeng, J., Xia, J., Xin, P., 2025. Effects of low-tide rainfall on channel morphodynamics of tidal mudflats. Estuar. Coast. Shelf Sci. 313. https://doi.org/10.1016/j.ecss.2024.109108.

Lefebvre, A., Ernstsen, V.B., Winter, C., 2013. Estimation of roughness lengths and flow separation over compound bedforms in a natural-tidal inlet. Cont. Shelf Res. 61, 98–111. https://doi.org/10.1016/j.csr.2013.04.030.

Leonardi, N., Carnacina, I., Donatelli, C., Ganju, N.K., Plater, A.J., Schuerch, M., Temmerman, S., 2018. Dynamic interactions between coastal storms and salt marshes: a review. Geomorphology. https://doi.org/10.1016/j.geomorph.2017.11.001.

Li, C., Peng, Z., Zhao, Y., Fang, D., Chen, X., Xu, F., Wang, X., 2024. Seasonal variations in drag coefficient of salt marsh vegetation. Coast. Eng. 193. https://doi.org/10.1016/j.coastaleng.2024.104575.

Li, T., Wu, P., Zuo, L., Yang, J., 2025. Impacts of tidal creek development on vegetation restoration during ecological water supplement in the Yellow River Delta. J. Geogr. Sci. 35 (6), 1365–1380. https://doi.org/10.1007/s11442-025-2371-y.

Luppi, T., Bas, C., Méndez Casariego, A., Albano, M., Lancia, J., Kittlein, M., et al., 2013. The influence of habitat, season and tidal regime in the activity of the intertidal crab Neohelice (=Chasmagnathus) granulata. Helgol. Mar. Res. 67 (1), 1–15. https://doi.org/10.1007/s10152-012-0300-9.

Ly, T.N., Huang, Z.C., 2022. Real-time and long-term monitoring of waves and suspended sediment concentrations over an intertidal algal reef. Environ. Monit. Assess. 194 (11). https://doi.org/10.1007/s10661-022-10491-0.

Mariotti, Giulio, Fagherazzi, S., 2010. A numerical model for the coupled long-term evolution of salt marshes and tidal flats. J. Geophys. Res. Earth Surf. 115 (1). https://doi.org/10.1029/2009JF001326.

Mariotti, Giulio, Fagherazzi, S., 2013. Critical width of tidal flats triggers marsh collapse in the absence of sea-level rise. Proc. Natl. Acad. Sci. USA 110 (14), 5353–5356. https://doi.org/10.1073/pnas.1219600110.

Mariotti, G., Fagherazzi, S., Wiberg, P.L., McGlathery, K.J., Carniello, L., Defina, A., 2010. Influence of storm surges and sea level on shallow tidal basin erosive processes. J. Geophys. Res. Oceans 115 (11). https://doi.org/10.1029/2009JC005892.

Mckew, B.A., Dumbrell, A.J., Taylor, J.D., Mcgenity, T.J., Underwood, G.J.C., 2013. Differences between aerobic and anaerobic degradation of microphytobenthic biofilm-derived organic matter within intertidal sediments. FEMS Microbiol. Ecol. 84 (3), 495–509. https://doi.org/10.1111/1574-6941.12077.

Meynecke, J.O., Lee, S.Y., Duke, N.C., Warnken, J., 2006. Effect of rainfall as a component of climate change on estuarine fish production in Queensland, Australia. Estuar. Coast. Shelf Sci. 69 (3–4), 491–504. https://doi.org/10.1016/j.ecss.2006.05.011.

Mok, J.S., Kim, S.H., Kim, J., Cho, H., An, S.U., Choi, A., et al., 2019. Impacts of typhoon-induced heavy rainfalls and resultant freshwater runoff on the partitioning of organic carbon oxidation and nutrient dynamics in the intertidal sediments of the Han River estuary, Yellow Sea. Sci. Total Environ. 691, 858–867. https://doi.org/10.1016/j.scitotenv.2019.07.031.

Morton, R.A., Barras, J.A., 2011. Hurricane impacts on coastal wetlands: a half-century record of storm-generated features from southern Louisiana. J. Coast. Res. 27 (6 A), 27–43. https://doi.org/10.2112/JCOASTRES-D-10-00185.1.

Murphy, S., Voulgaris, G., 2006. Identifying the role of tides, rainfall and seasonality in marsh sedimentation using long-term suspended sediment concentration data. Mar. Geol. 227 (1–2), 31–50. https://doi.org/10.1016/j.margeo.2005.10.006.

Murray, N.J., Phinn, S.R., DeWitt, M., Ferrari, R., Johnston, R., Lyons, M.B., et al., 2019. The global distribution and trajectory of tidal flats. Nature 565 (7738), 222–225. https://doi.org/10.1038/s41586-018-0805-8.

Novakowski, K.I., Torres, R., Gardner, L.R., Voulgaris, G., 2004. Geomorphic analysis of tidal creek networks. Water Resour. Res. 40 (5). https://doi.org/10.1029/2003WR002722.

Nowacki, D.J., Ganju, N.K., 2019. Simple metrics predict salt-marsh sediment fluxes. Geophys. Res. Lett. 46 (21), 12250–12257. https://doi.org/10.1029/2019GL083819.

Orvain, F., De Crignis, M., Guizien, K., Lefebvre, S., Mallet, C., Takahashi, E., Dupuy, C., 2014. Tidal and seasonal effects on the short-term temporal patterns of bacteria, microphytobenthos and exopolymers in natural intertidal biofilms (Brouage, France). J. Sea Res. 92, 6–18. https://doi.org/10.1016/j.seares.2014.02.018.

Pan, S., Gong, Z., Geng, L., Han, G., 2025. How erosion of salt marsh edges leads to the loss of organic carbon: insights from Jiangsu coast, China. Ocean Coast. Manag. 264. https://doi.org/10.1016/j.ocecoaman.2025.107642.

Pannozzo, N., Leonardi, N., Carnacina, I., Smedley, R., 2021. Salt marsh resilience to sea-level rise and increased storm intensity. Geomorphology 389. https://doi.org/10.1016/j.geomorph.2021.107825.

Pethick, J.S., 1981. Long-term accretion rates on tidal salt marshes. J. Sediment. Res. 51 (2), 571–577. https://doi.org/10.1306/212F7CDE-2B24-11D7-8648000102C1865D.

Pieterse, A., Puleo, J.A., McKenna, T.E., 2016. Hydrodynamics and sediment suspension in shallow tidal channels intersecting a tidal flat. Cont. Shelf Res. 119, 40–55. https://doi.org/10.1016/j.csr.2016.03.012.

Ranasinghe, R., Pattiaratchi, C., Masselink, G., 1999. A morphodynamic model to simulate the seasonal closure of tidal inlets. Coast. Eng. (Amst.) 37 (1), 1–36. https://doi.org/10.1016/S0378-3839(99)00008-3.

Rinaldo, A., Fagherazzi, S., Lanzoni, S., Marani, M., Dietrich, W.E., 1999. Tidal networks 2. Watershed delineation and comparative network morphology. Water Resour. Res. 35 (12), 3905–3917. https://doi.org/10.1029/1999WR900237.

Rios-Yunes, D., Grandjean, T., di Primio, A., Tiano, J., Bouma, T.J., van Oevelen, D., Soetaert, K., 2023. Sediment resuspension enhances nutrient exchange in intertidal mudflats. Front. Mar. Sci. 10. https://doi.org/10.3389/fmars.2023.1155386.

Sakamaki, T., Nishimura, O., 2006. Dynamic equilibrium of sediment carbon content in an estuarine tidal flat: characterization and mechanisms. Mar. Ecol. Prog. Ser. 29–40.

Sakamaki, T., Nishimura, O., 2007. Physical control of sediment carbon content in an estuarine tidal flat system (Nanakita River, Japan): a mechanistic case study. Estuar. Coast. Shelf Sci. 73 (3–4), 781–791. https://doi.org/10.1016/j.ecss.2007.03.019.

Sasmito, S.D., Kuzyakov, Y., Lubis, A.A., Murdiyarso, D., Hutley, L.B., Bachri, S., et al., 2020. Organic carbon burial and sources in soils of coastal mudflat and mangrove ecosystems. Catena 187. https://doi.org/10.1016/j.catena.2019.104414.

Seminara, G., Bolla Pittaluga, M., Tambroni, N., 2004. Long term morphodynamic equilibrium of tidal channels. In: Shallow Flows. Taylor & Francis, pp. 207–216. https://doi.org/10.1201/9780203027325.ch26.

Seneviratne, S.I., Zhang, X., Adnan, M., Badi, W., Dereczynski, C., Luca, A. Di, et al., 2021. Weather and Climate Extreme Events in a Changing Climate.

Shi, B.W., Yang, S.L., Wang, Y.P., Bouma, T.J., Zhu, Q., 2012. Relating accretion and erosion at an exposed tidal wetland to the bottom shear stress of combined current-wave action. Geomorphology 138 (1), 380–389. https://doi.org/10.1016/j.geomorph.2011.10.004.

Shi, B.W., Yang, S.L., Wang, Y.P., Li, G.C., Li, M.L., Li, P., Li, C., 2017. Role of wind in erosion-accretion cycles on an estuarine mudflat. J. Geophys. Res. Oceans 122 (1), 193–206. https://doi.org/10.1002/2016JC011902.

Shi, B., Yang, S.L., Temmerman, S., Bouma, T., Ysebaert, T., Wang, S., et al., 2021. Effect of typhoon-induced intertidal-flat erosion on dominant macrobenthic species (Meretrix meretrix). Limnol. Oceanogr. 66 (12), 4197–4209. https://doi.org/10.1002/lno.11953.

Soulsby, R.L., Clarke, S., 2005. Bed Shear-stresses Under Combined Waves and Currents on Smooth and Rough Beds.

Speer, M.S., Leslie, L.M., Fierro, A.O., 2011. Australian east coast rainfall decline related to large scale climate drivers. Clim. Dyn. 36 (7–8), 1419–1429. https://doi.org/10.1007/s00382-009-0726-1.

Spivak, A.C., Sanderman, J., Bowen, J.L., Canuel, E.A., Hopkinson, C.S., 2019. Global-change controls on soil-carbon accumulation and loss in coastal vegetated ecosystems. Nat. Geosci. 12 (9), 685–692. https://doi.org/10.1038/s41561-019-0435-2.

Steinmuller, H.E., Dittmer, K.M., White, J.R., Chambers, L.G., 2019. Understanding the fate of soil organic matter in submerging coastal wetland soils: a microcosm approach. Geoderma 337, 1267–1277. https://doi.org/10.1016/j.geoderma.2018.08.020.

Sumner, G., Homar, V., Ramis, C., 2001. Precipitation seasonality in eastern and southern coastal Spain. Int. J. Climatol. 21 (2), 219–247. https://doi.org/10.1002/joc.600.

Sun, J., van Prooijen, B., Wang, X., Hanssen, J., Xie, W., Lin, J., et al., 2024a. Sources of suspended sediments in salt marsh creeks: Field measurements in China and the Netherlands. Geomorphology 456. https://doi.org/10.1016/j.geomorph.2024.109206.

Sun, J., van Prooijen, B., Wang, X., Zhao, Z., He, Q., Wang, Z., 2024b. Sediment fluxes within salt marsh tidal creek systems in the Yangtze Estuary. Geomorphology 449. https://doi.org/10.1016/j.geomorph.2023.109031.

Sun, J., van Prooijen, B., Wang, X., Xie, W., Xu, F., He, Q., Wang, Z., 2024c. Conditional effects of tides and waves on sediment supply to salt marshes. J. Geophys. Res. Earth 129 (10). https://doi.org/10.1029/2024JF007686.

Talke, S.A., Stacey, M.T., 2008. Suspended sediment fluxes at an intertidal flat: the shifting influence of wave, wind, tidal, and freshwater forcing. Cont. Shelf Res. 28 (6), 710–725. https://doi.org/10.1016/j.csr.2007.12.003.

Te Slaa, S., He, Q., Van Maren, D.S., Winterwerp, J.C., 2013. Sedimentation processes in silt-rich sediment systems Topical Collection on the 11th International Conference on Cohesive Sediment Transport. Ocean Dyn. 63 (4), 399–421. https://doi.org/10.1007/s10236-013-0600-x.

Temmerman, S., Meire, P., Bouma, T.J., Herman, P.M.J., Ysebaert, T., De Vriend, H.J., 2013. Ecosystem-based coastal defence in the face of global change. Nature. https://doi.org/10.1038/nature12859.

Tognin, D., D'Alpaos, A., Marani, M., Carniello, L., 2021. Marsh resilience to sea-level rise reduced by storm-surge barriers in the Venice Lagoon. Nat. Geosci. 14 (12), 906–911. https://doi.org/10.1038/s41561-021-00853-7.

Tolhurst, T.J., Friend, P.L., Watts, C., Wakefield, R., Black, K.S., Paterson, D.M., 2006. The effects of rain on the erosion threshold of intertidal cohesive sediments. Aquat. Ecol. 40 (4), 533–541. https://doi.org/10.1007/s10452-004-8058-z.

Tseng, K.H., Kuo, C.Y., Lin, T.H., Huang, Z.C., Lin, Y.C., Liao, W.H., Chen, C.F., 2017. Reconstruction of time-varying tidal flat topography using optical remote sensing imageries. ISPRS J. Photogramm. Remote Sens. 131, 92–103. https://doi.org/10.1016/j.isprsjprs.2017.07.008.

Voulgaris, G., Meyers, S.T., 2004. Net effect of rainfall activity on salt-marsh sediment distribution. Mar. Geol. 207 (1–4), 115–129. https://doi.org/10.1016/j.margeo.2004.03.009.

Wang, X., Sun, J., Zhao, Z., 2020. Effects of river discharge and tidal meandering on morphological changes in a meso tidal creek. Estuar. Coast. Shelf Sci. 234. https://doi.org/10.1016/j.ecss.2020.106635.

Whitehouse, R.J.S., Bassoullet, P., Dyer, K.R., Mitchener, H.J., Roberts, W., 2000. The influence of bedforms on flow and sediment transport over intertidal mudflats. Cont. Shelf Res. 20, 1099–1124.

Xie, W., He, Q., Zhang, K., Guo, L., Wang, X., Shen, J., Cui, Z., 2017. Application of terrestrial laser scanner on tidal flat morphology at a typhoon event timescale. Geomorphology 292, 47–58. https://doi.org/10.1016/j.geomorph.2017.04.034.

Xie, W., He, Q., Wang, X., Guo, L., Zhang, K., 2018. Role of mudflat-creek sediment exchanges in intertidal sedimentary processes. J. Hydrol. 567, 351–360. https://doi.org/10.1016/j.jhydrol.2018.10.027.

Xie, W., Wang, X., Guo, L., He, Q., Dou, S., Yu, X., 2021. Impacts of a storm on the erosion process of a tidal wetland in the Yellow River Delta. Catena 205. https://doi.org/10.1016/j.catena.2021.105461.

Xin, P., Zhou, T., Lu, C., Shen, C., Zhang, C., D'Alpaos, A., Li, L., 2017. Combined effects of tides, evaporation and rainfall on the soil conditions in an intertidal creek-marsh system. Adv. Water Resour. 103, 1–15. https://doi.org/10.1016/j.advwatres.2017.02.014.

Yang, S.L., Li, H., Ysebaert, T., Bouma, T.J., Zhang, W.X., Wang, Y.Y., et al., 2008. Spatial and temporal variations in sediment grain size in tidal wetlands, Yangtze Delta: on the role of physical and biotic controls. Estuar. Coast. Shelf Sci. 77 (4), 657–671. https://doi.org/10.1016/j.ecss.2007.10.024.

Young, I.R., Verhagen, L.A., 1996. Coastal engineering the growth of fetch limited waves in water of finite depth. Part 1. Total energy and peak frequency. Coast. Eng. 29.

Zhan, Y., Aarninkhof, S.G.J., Wang, Z., Qian, W., Zhou, Y., 2019. Daily topographic change patterns of tidal flats in response to anthropogenic activities: analysis through coastal video imagery. J. Coast. Res. 36 (1), 103–115. https://doi.org/10.2112/JCOASTRES-D-18-00117.1.

Zhou, Z., Liang, M. Jiao, Chen, L., Xu, M. Piao, Chen, X., Geng, L., et al., 2022. Processes, feedbacks, and morphodynamic evolution of tidal flat–marsh systems: progress and challenges. Water Sci. Eng. 15 (2), 89–102. https://doi.org/10.1016/j.wse.2021.07.002.

Zhu, J., Olsen, C.R., 2014. Sedimentation and organic carbon burial in the Yangtze River and Hudson river estuaries: implications for the global carbon budget. Aquat. Geochem. 20 (2–3), 325–342. https://doi.org/10.1007/s10498-013-9191-x.

Zhu, Q., van Prooijen, B.C., Wang, Z.B., Ma, Y.X., Yang, S.L., 2016. Bed shear stress estimation on an open intertidal flat using in situ measurements. Estuar. Coast. Shelf Sci. 182, 190–201. https://doi.org/10.1016/j.ecss.2016.08.028.

Žydelis, R., Dorsch, M., Heinänen, S., Nehls, G., Weiss, F., 2019. Comparison of digital video surveys with visual aerial surveys for bird monitoring at sea. J. Ornithol. 160 (2), 567–580. https://doi.org/10.1007/s10336-018-1622-4.